



# Propagation Characteristics of Two Coronal Mass Ejections from the Sun Far into Interplanetary Space

Xiaowei Zhao<sup>1,2</sup>, Ying D. Liu<sup>1,2</sup>, Huidong Hu<sup>1,2</sup>, and Rui Wang<sup>1</sup>

<sup>1</sup> State Key Laboratory of Space Weather, National Space Science Center, Chinese Academy of Sciences, Beijing 100190, China; [liuxying@spaceweather.ac.cn](mailto:liuxying@spaceweather.ac.cn)

<sup>2</sup> University of Chinese Academy of Sciences, Beijing 100049, China

Received 2016 December 21; revised 2017 January 25; accepted 2017 February 3; published 2017 February 27

## Abstract

Propagation of coronal mass ejections (CMEs) from the Sun far into interplanetary space is not well understood, due to limited observations. In this study we examine the propagation characteristics of two geo-effective CMEs, which occurred on 2005 May 6 and 13, respectively. Significant heliospheric consequences associated with the two CMEs are observed, including interplanetary CMEs (ICMEs) at the Earth and *Ulysses*, interplanetary shocks, a long-duration type II radio burst, and intense geomagnetic storms. We use coronagraph observations from *SOHO*/LASCO, frequency drift of the long-duration type II burst, in situ measurements at the Earth and *Ulysses*, and magnetohydrodynamic propagation of the observed solar wind disturbances at 1 au to track the CMEs from the Sun far into interplanetary space. We find that both of the CMEs underwent a major deceleration within 1 au and thereafter a gradual deceleration when they propagated from the Earth to deep interplanetary space, due to interactions with the ambient solar wind. The results also reveal that the two CMEs interacted with each other in the distant interplanetary space even though their launch times on the Sun were well separated. The intense geomagnetic storm for each case was caused by the southward magnetic fields ahead of the CME, stressing the critical role of the sheath region in geomagnetic storm generation, although for the first case there is a corotating interaction region involved.

**Key words:** shock waves – solar wind – Sun: coronal mass ejections (CMEs) – Sun: heliosphere – Sun: radio radiation

## 1. Introduction

Coronal mass ejections (CMEs) are large eruptions of plasma and magnetic fields from the solar corona and can cause severe space weather effects. Interplanetary CMEs (ICMEs) are regarded as the heliospheric counterpart of CMEs. ICMEs are often associated with interplanetary shocks and prolonged southward components of magnetic fields. A southward field component can reconnect with the dayside geomagnetic fields and trigger geomagnetic storms (Dungey 1961; Gonzalez et al. 1994; Tsurutani & Gonzalez 1997). Although the source regions of CMEs and their propagation within 1 au have been extensively studied, their evolution in the deep interplanetary space is not well understood, due to the limitation of observations. Multi-spacecraft remote sensing and in situ observations are crucial for understanding the propagation of CMEs in interplanetary space.

Previous studies indicate that different types of CMEs may have different propagation histories. Fast CMEs may undergo a deceleration while slow CMEs are accelerated due to interactions with the ambient solar wind (Sheeley et al. 1999; Gopalswamy et al. 2000). Empirical models combining coronagraph observations and in situ measurements have been proposed to investigate the propagation of CMEs within 1 au (Lindsay et al. 1999; Gopalswamy et al. 2001a). Gopalswamy et al. (2001a) suggest that CMEs experience a deceleration out to 0.76 au and then they move with a constant speed. These studies are based on coronagraph observations, whose field of view is limited to 30  $R_{\odot}$ . A propagation model has been proposed using the frequency drift of interplanetary type II radio bursts to invert the distance of CME-driven shocks (Reiner et al. 2007; Liu et al. 2008). Based on a statistical analysis of interplanetary type II radio bursts, Reiner et al.

(2007) argue that the deceleration cessation distances of CMEs range from 0.3 au to beyond 1 au. Doppler scintillation measurements of shock locations and speeds indicate that fast shocks may experience substantial deceleration near the Sun (Woo et al. 1985; Woo 1988). Cane et al. (1986) suggest that fast shocks may decelerate rapidly while slow shocks propagate at about constant speed, based on the comparison between the result of Woo et al. (1985) and in situ measurements at *Helios*. Combining coronagraph observations, type II radio bursts, interplanetary scintillation technique (IPS), and in situ observations at *Wind*, Gonzalez-Esparza & Aguilar-Rodriguez (2009) argue that CMEs/shocks undergo a gradual deceleration within 1 au. A general picture of Sun-to-Earth propagation of fast CMEs (with speeds above 1000 km s<sup>-1</sup>) has been found by Liu et al. (2013), combining stereoscopic wide-angle heliocentric imaging observations from *STEREO*, interplanetary type II radio bursts, and in situ measurements at 1 au. They reveal that fast CMEs experience an impulsive acceleration, then decelerate in a relatively short timescale, and finally move with a roughly constant speed or a gradual deceleration. Liu et al. (2016) further provide the propagation characteristics of slow CMEs (with speeds below 400 km s<sup>-1</sup>) in the Sun–Earth space. They find that slow CMEs are gradually accelerated to the ambient solar wind speed around 20–30 solar radii and then comove with the solar wind.

Interplanetary propagation of CMEs can be influenced by their interactions with solar wind structures, including other CMEs (e.g., Gopalswamy et al. 2001b; Liu et al. 2012, 2014a; Lugaz et al. 2012; Temmer et al. 2012), which will make their propagation more complex. Temmer et al. (2012) find that a fast CME can be significantly slowed down by interacting with another CME. A CME can also be deflected by interacting with other CMEs in the corona and interplanetary space

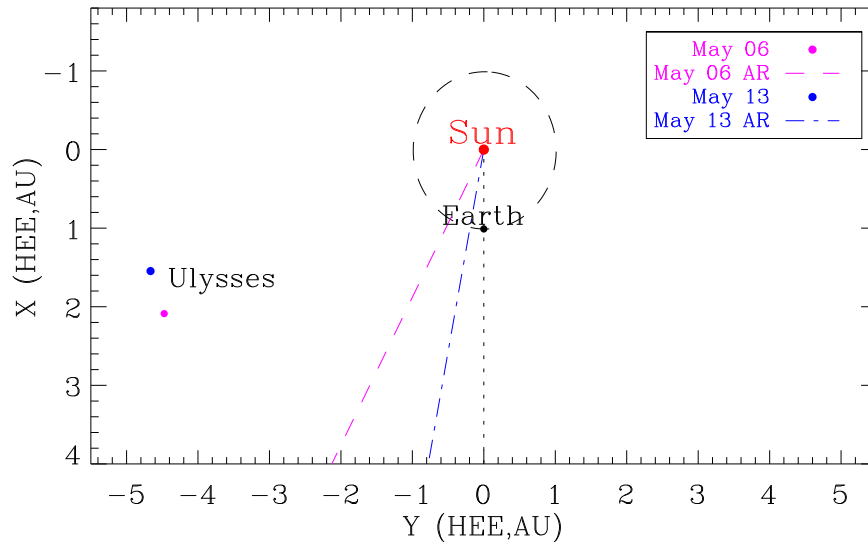


**Figure 1.** Positions of *Ulysses* and the Earth in the ecliptic plane. The dashed curve indicates the orbit of the Earth. The purple dashed line and the purple dot represent the longitude of the active region and the position of *Ulysses* projected onto the ecliptic corresponding to the 2005 May 6 CME, respectively. The blue dotted–dashed line and the blue dot indicate the longitude of the active region and the projected position of *Ulysses* corresponding to the 2005 May 13 CME, respectively.

(Gopalswamy et al. 2001b; Lugaz et al. 2012; Liu et al. 2014a). Liu et al. (2014a) suggest that an earlier CME can remove some of the solar wind plasma and give rise to a modest deceleration of the later CME, which they call “preconditioning.” The importance of the preconditioning of the upstream solar wind for CME propagation has been confirmed by Temmer & Nitta (2015) and Cash et al. (2015). Other solar wind structures, such as high-speed streams, can change CME propagation in a similar way. For example, slow CMEs can be accelerated by high-speed streams from behind (Kataoka et al. 2015; Liu et al. 2015, 2016).

CME kinematics can be obtained by combining multi-spacecraft remote sensing and in situ observations with different modeling techniques. Thernisien et al. (2006) have proposed a Graduated Cylindrical Shell (GCS) model to reconstruct CMEs. The GCS model can acquire the heliocentric distances of the CME leading front and has been successfully applied to *SOHO* and *STEREO* imaging observations (e.g., Thernisien et al. 2009; Liu et al. 2010; Cheng et al. 2013; Mishra et al. 2015). The frequency drift of type II radio bursts produced by CME-driven shocks can be converted to radial distances using a proper solar wind density model (e.g., Reiner et al. 2007; Liu et al. 2008, 2013; Cremades et al. 2015; Hu et al. 2016). Using the electron density model of Leblanc et al. (1998, referred to as the Leblanc density model hereafter), Liu et al. (2013) obtain the radial distances of CME-driven shocks from type II burst observations and find general consistency with those derived from triangulation techniques based on *STEREO* imaging observations. Liu et al. (2008) have investigated the propagation of a CME/shock from the Sun far into interplanetary space by combining the frequency drift of type II radio emissions, in situ observations at 1 au and *Ulysses*, and a magnetohydrodynamic (MHD) model. Richardson (2014) compares the speeds of 11 ICMEs at the Earth and *Ulysses* and suggests that ICMEs with speeds above the solar wind at the Earth continue to decelerate out to *Ulysses*, although at a slower rate than in the Sun–Earth space. Based on the derived CME/shock kinematics, we can estimate their arrival times at the Earth and investigate their interplanetary propagation characteristics.

The main purpose of this paper is to investigate the propagation and evolution of two geo-effective CMEs in the heliosphere, which occurred on 2005 May 6 and 13, respectively. The two CMEs are well observed by a fleet of spacecraft, including coronagraph observations from *SOHO*/LASCO, in situ measurements at the Earth and *Ulysses*, and a long-duration type II burst from *Wind*. This provides a great opportunity to study the propagation of CMEs from the Sun to deep interplanetary space. We combine these different data sets with modeling techniques to give a comprehensive view of the two geo-effective CMEs. Although there are some previous studies looking at the 2005 May 13 CME individually (e.g., Yurchyshyn et al. 2006; Reiner et al. 2007; Bisi et al. 2010; Gopalswamy 2010; Manchester et al. 2014), we study the two geo-effective CMEs together and pay particular attention to the propagation characteristics of the two CMEs from the Sun far into interplanetary space. It is also interesting to show that although the launch times of the two CMEs are well separated, the CMEs can still interact with each other in interplanetary space. We illustrate how the arrival time of a CME/shock can be estimated at the Earth using merged remote-sensing observations, which is important for space weather forecasting. We examine coronagraph observations in Section 2 and heliospheric consequences in Section 3. The results are summarized and discussed in Section 4.

## 2. CMEs at the Sun

On 2005 May 6, a CME (CME1) was launched from NOAA AR 10758 (S07°E28°), associated with a C8.5 flare that peaked at about 17:05 UT. There is no clear interplanetary type II burst accompanying this CME. Another CME (CME2) erupted on 2005 May 13 from NOAA AR 10759 (N12°E11°), approximately a week after the eruption of CME1. It was associated with a long-duration M8.0 flare that peaked at around 16:57 UT.

Figure 1 shows the configuration of the planets and spacecraft in the ecliptic plane. The longitudes of the active regions (ARs) of CME1 and CME2 are also indicated in this figure. When the two CMEs erupted from the Sun, the

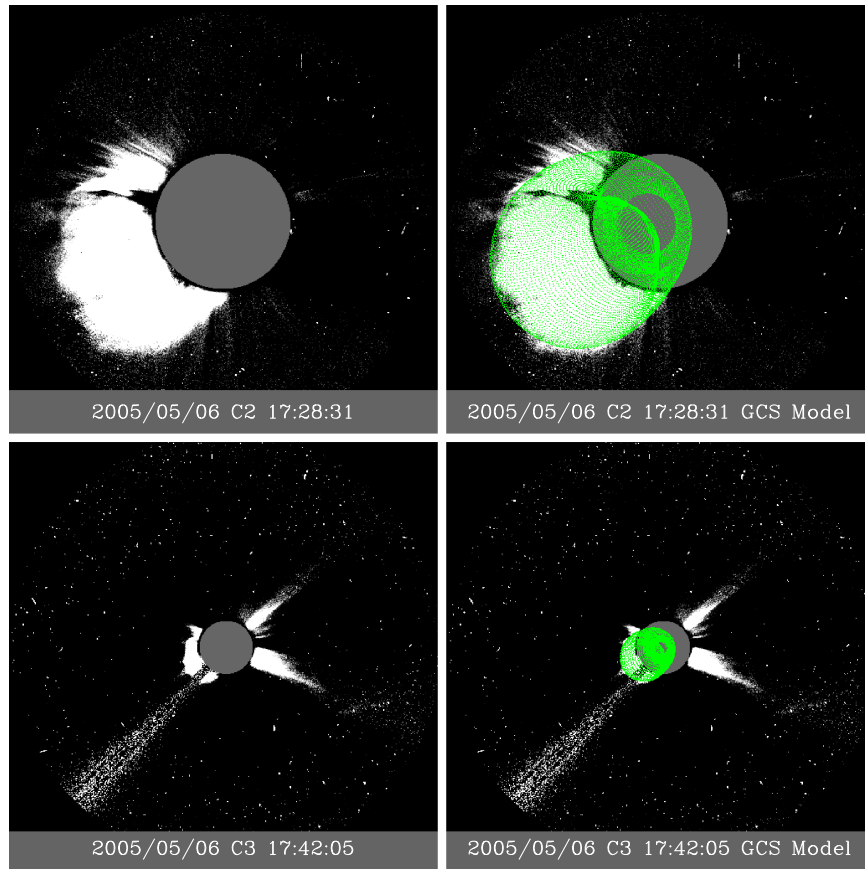


**Figure 2.** Coronagraph running-difference observations and modeling of the 2005 May 6 CME. The left column shows the observations from LASCO C2 (upper) and C3 (lower), and the right column the GCS modeling (green grids) overlapped on the observed images.

longitudinal difference between the Earth and *Ulysses* for CME1 and CME2 was about  $64.7^\circ$  and  $71.3^\circ$ , respectively. Although the launch times of the two CMEs are well separated, they are likely to interact in interplanetary space since the ARs were at similar longitudes with respect to the Earth/*Ulysses* and CME2 is faster than CME1 (see the text below). The CMEs would impact the Earth and perhaps *Ulysses* as well.

The coronagraph observations and modeling of CME1 are displayed in Figure 2. This is a partial halo CME, which is consistent with its solar source longitude ( $E28^\circ$ ). We use the GCS model proposed by Thernisien et al. (2006) to reproduce CME1 at different times based on the observations, which can give the heliocentric distances of the CME1 leading front. This model has six free parameters: the longitude and latitude of the propagation direction, the tilt angle, aspect ratio and half angle of the flux rope, and the height of the CME leading front. While using this model, we keep the tilt angle, aspect ratio, and half angle parameters constant, and adjust the longitude and latitude. We see good visual consistency between the wireframe rendering obtained from the GCS model and the observed images. Applying the GCS model to single spacecraft observations may give rise to large uncertainties in the parameters. All the resulting parameters of the reconstruction are listed in Table 1. The flux-rope tilt angle is chosen to be consistent with the orientation of the neutral line in the AR. The longitude of the propagation direction agrees with the solar source longitude ( $E28^\circ$ ). The latitude is also consistent with the solar source latitude ( $S07^\circ$ ), although a slight southward transition may be present. The speed of the CME, obtained

with a linear fit of the CME leading front distances obtained from the GCS fit, is about  $1300 \text{ km s}^{-1}$ .

Figure 3 shows the coronagraph observations and modeling of CME2. This is a halo CME, and only two frames of images are available from LASCO. We also obtain a good visual agreement between the model results and the images of CME2. The tilt angle, again, is chosen to be consistent with the neutral line orientation in the AR inferred from magnetogram observations (Yurchyshyn et al. 2006). The longitude of the CME propagation direction also agrees with the solar source longitude ( $E11^\circ$ ). The latitude shows a small southward transition compared with the solar source latitude ( $N12^\circ$ ). The CME speed, estimated with a linear fit of the two distances, is about  $2485 \text{ km s}^{-1}$ . The error of the speed may be large, as we only have two data points.

### 3. Heliospheric Consequences

#### 3.1. ICMEs at the Earth and Geo-effectiveness

We associate the two CMEs with their interplanetary counterparts at 1 au based on their transit times from the Sun to the Earth. Figure 4 presents the in situ measurements of CME1 by *Wind* and *ACE* near the Earth. There are no clear shock signatures ahead of the ICME. The shaded region indicates the ICME with an interval from 18:00 UT on May 8 to 04:33 UT on May 11. The ICME interval is mainly determined from the smooth magnetic field and the depressed proton temperature compared with the expected temperature. The use of the expected temperature for the identification of



**Table 1**  
CME Parameters Obtained from the GCS Model

CMEs	Coronagraph	Time	Lon ( $^{\circ}$ ) <sup>a</sup>	Lat ( $^{\circ}$ ) <sup>a</sup>	Tilt Angle	Aspect Ratio	Half Angle	Height ( $R_{\odot}$ ) <sup>b</sup>
CME1	C2	17:28	-35.78	-15.65	35.78	0.674	15.93	6.58
	C2	17:54	-32.42	-15.65	35.78	0.674	15.93	9.65
	C3	17:42	-28	-14.54	35.78	0.674	15.93	8.39
	C3	18:18	-28	-14.54	35.78	0.674	15.93	13.16
	C3	18:42	-28	-16.77	35.78	0.674	15.93	15.77
	C3	19:42	-28	-19.01	35.78	0.674	15.93	22.71
	C3	20:18	-28	-22.36	35.78	0.674	15.93	25.05
	C3	20:42	-28	-22.36	35.78	0.674	15.93	28.56
CME2	C2	17:22	-1.12	-1.12	-43.04	0.696	9.78	10.10
	C3	17:42	-2.24	-1.68	-43.04	0.696	9.78	14.42

**Notes.**

<sup>a</sup> Longitude and latitude in the heliographic coordinates.

<sup>b</sup> The heliocentric distances of the CME leading front at different times.

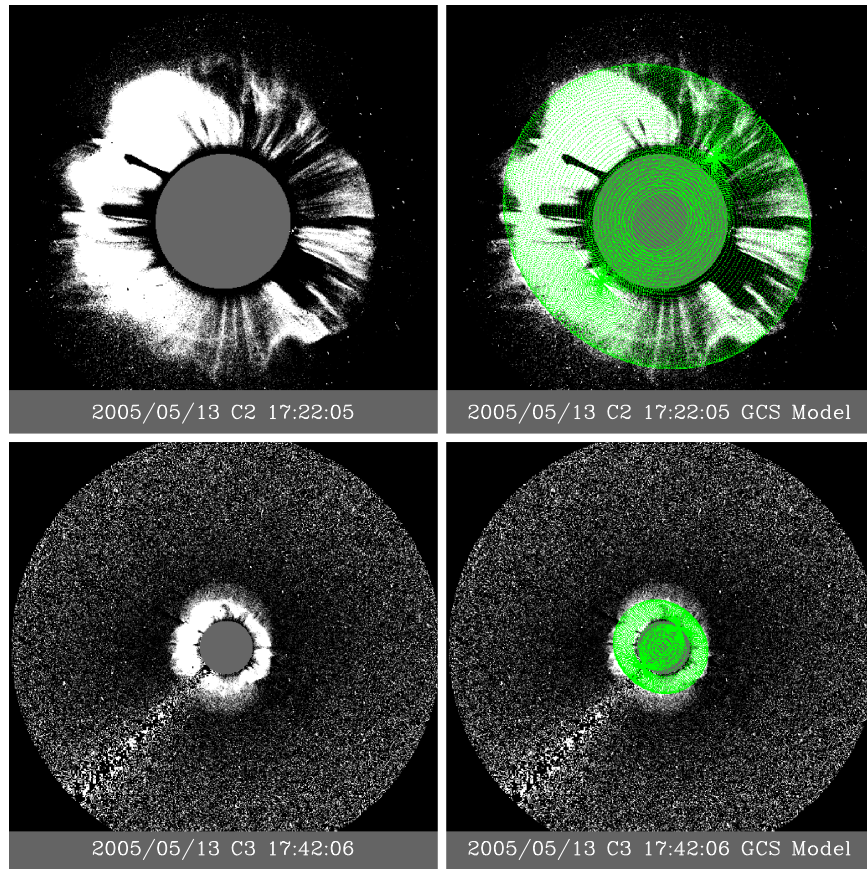


**Figure 3.** Similar to Figure 2, but for the coronagraph running-difference observations and modeling of the 2005 May 13 CME.

ICMEs is introduced by Richardson & Cane (1993, 1995) based on the solar wind temperature–speed relationship developed by Lopez & Freeman (1986). The alpha-to-proton density ratio is enhanced but patchy inside the ICME. Zhang et al. (2007) suggest that the solar wind structure ahead of the ICME is a corotating interaction region (CIR). The average solar wind speed across the ICME leading edge is about  $750 \text{ km s}^{-1}$ . Through comparing the speed of the ICME leading edge with that measured by *SOHO*/LASCO ( $1300 \text{ km s}^{-1}$ ), we suggest that CME1 must have decelerated within 1 au. An intense geomagnetic storm occurred with a minimum value of the  $D_{st}$  index of  $-110 \text{ nT}$ . The southward field component

inside the ICME is small (see the second panel from the bottom in Figure 4). The intense geomagnetic storm is induced by the southward field components in the CIR ahead of the ICME (Zhang et al. 2007), although the southward field components are fluctuating. The ICME may have contributed to the geomagnetic storm by compressing the CIR from behind.

Figure 5 shows in situ *Wind* and *ACE* measurements of the 2005 May 13 CME (CME2). We can see a shock preceding the ICME at about 02:09 UT on May 15 inferred from the sharp increases in the solar wind plasma and magnetic field parameters. The position where the proton density, speed, temperature, and the magnetic field strength begin to decline

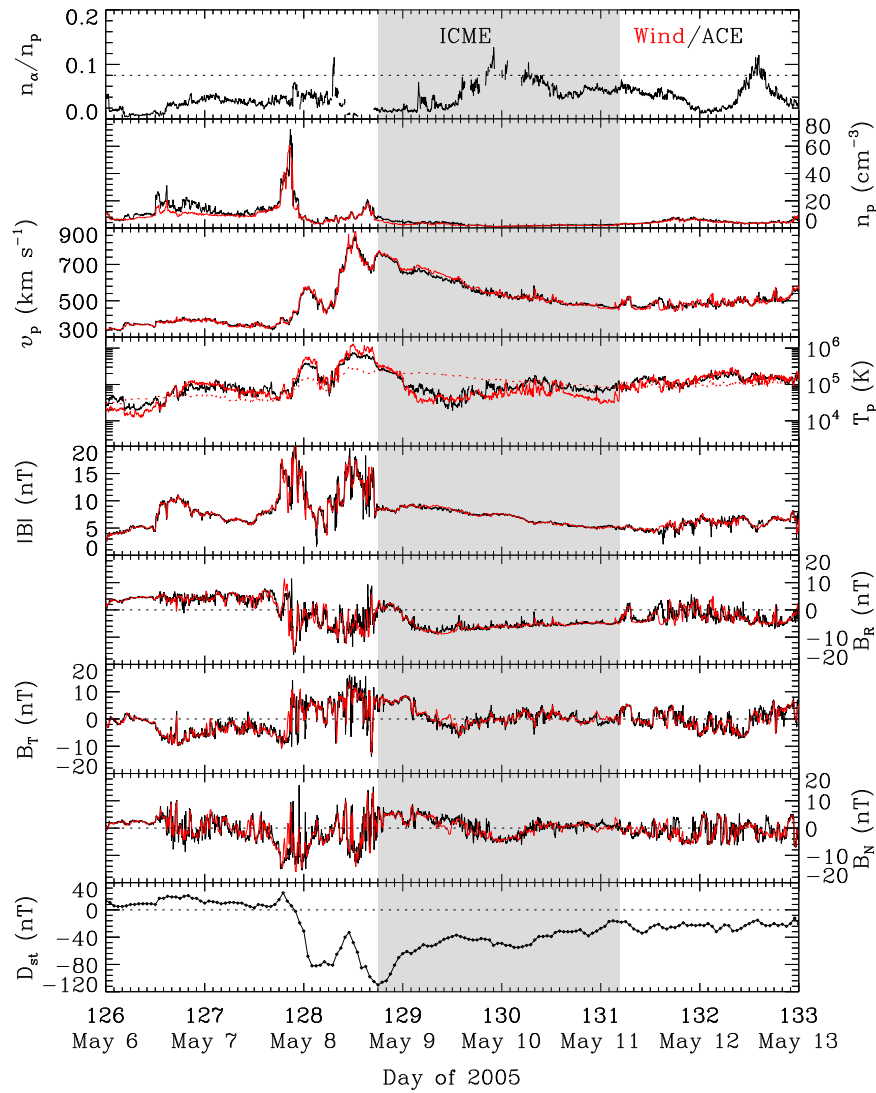


**Figure 4.** Solar wind measurements of CME1 at *Wind* (red) and *ACE* (black). From top to bottom, the panels show the density ratio between alphas and protons, proton density, bulk speed, proton temperature, magnetic field strength and components, and  $D_{st}$  index, respectively. The shaded region indicates the ICME interval. The dotted horizontal line in the first panel marks the 0.08 level of the alpha-to-proton density ratio, which is often used as a threshold for ICMEs (Richardson & Cane 2004; Liu et al. 2005, 2006b). The dotted curve in the fourth panel denotes the expected proton temperature from the speed observed by *Wind*.

indicates the ICME leading edge. It is difficult to determine the trailing boundary of the ICME interval, as the plasma and magnetic field parameters do not give a consensus on that. We tentatively suggest 12:00 UT on May 17 for the trailing boundary based on the depressed proton temperature, but 03:36 UT on May 19 is also possible considering the sustained period of the enhanced alpha-to-proton density ratio although the interval seems too long in this case. The transit time of CME2 from its eruption to the arrival of the shock at 1 au is about 33.5 hr, which gives an average speed of about  $1240 \text{ km s}^{-1}$ . We calculate the shock speed near the Earth with a simplified equation of conservation of mass:

$$v_s = \frac{n_2 v_2 - n_1 v_1}{n_2 - n_1}, \quad (1)$$

where  $n_1$  and  $n_2$  are the average densities and  $v_1$  and  $v_2$  are the average speeds upstream and downstream of the shock, respectively. Comparison between the average transit speed of CME2 ( $\sim 1240 \text{ km s}^{-1}$ ), the LASCO speed ( $\sim 2485 \text{ km s}^{-1}$ ), and the shock speed near the Earth ( $\sim 950 \text{ km s}^{-1}$ ) suggests that

the shock must undergo a deceleration when it propagates in the Sun–Earth space. A very severe geomagnetic storm with a minimum value of the  $D_{st}$  index of  $-247 \text{ nT}$ , seems caused by the enhanced southward magnetic field in the sheath region between the shock and ICME in combination with the high speed there. Given the uncertainty in determining the ICME leading edge, the southward field component causing the geomagnetic storm may be partly from inside the ICME. The southward field component is as large as  $-47 \text{ nT}$  in this case.

### 3.2. ICMEs at *Ulysses*

*Ulysses* was at a distance of  $\sim 5.08 \text{ au}$  from the Sun and  $\sim 21.4^\circ$  south and  $\sim 80^\circ$  east of the Earth, when it observed the 2005 May 6 and 13 CMEs. The positions of *Ulysses* projected onto the ecliptic plane corresponding to the two events are plotted on Figure 1. *Ulysses* might have observed both of the CMEs given that the longitudes of the ARs are not far away from it. Figure 6 displays solar wind measurements by *Ulysses*. We identify two ICMEs as shown by the shaded regions from

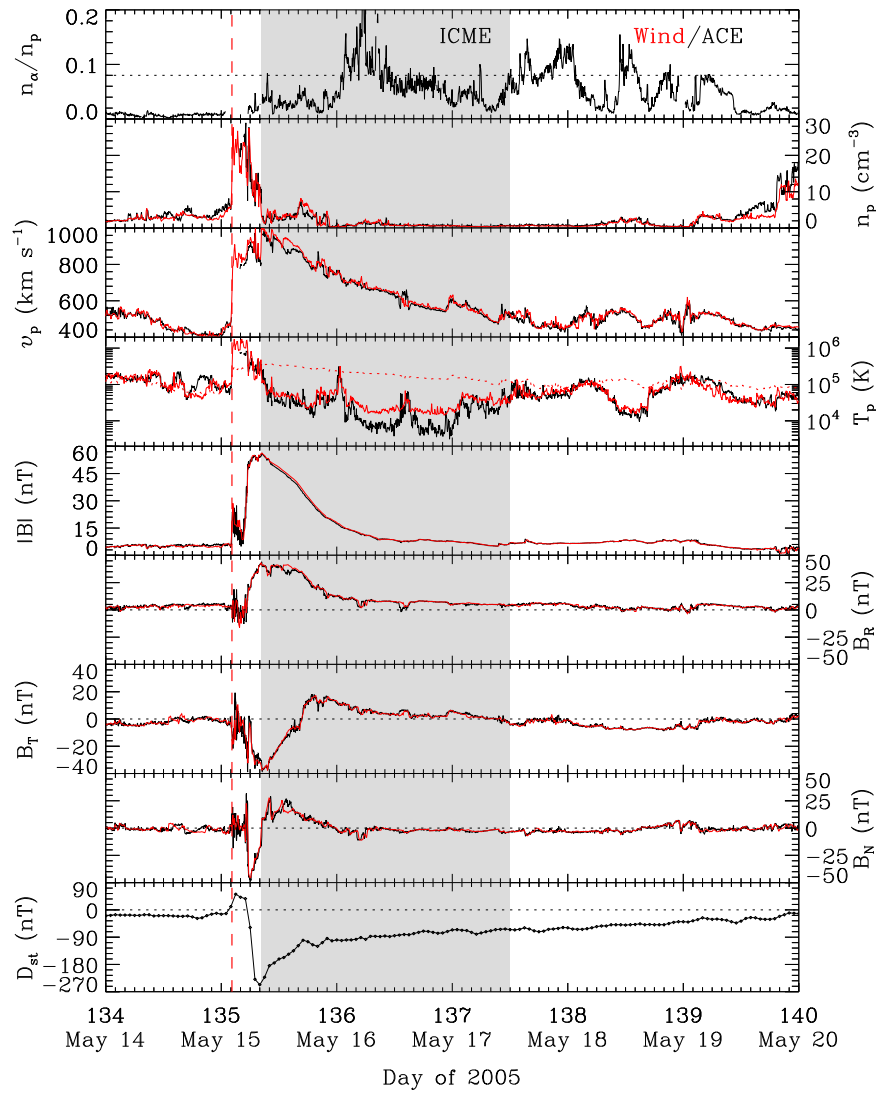


**Figure 5.** Similar to Figure 4, but for the in situ measurements of CME2. The red vertical dashed line marks the arrival time of the shock.

May 19 to May 26, which agree with the intervals of magnetic clouds (MCs) given by Du et al. (2010) and Richardson (2014). The first ICME (ICME1) is mainly determined from the enhanced magnetic field and rotation of the field, which is likely the in situ counterpart of the 2005 May 6 CME (CME1) according to the transit speed (see the text below). The signatures of the magnetic field components of ICME1 at *Wind* and *Ulysses* are not the same, perhaps due to the longitudinal separation between the two spacecraft so that they observe different parts of ICME1. It is also possible that the CME was modified during transit from 1 au to *Ulysses*. There is a shock-like structure preceding ICME1. The transit time of ICME1 from the Earth to *Ulysses* is about 10 days, which implies an average speed of about  $708 \text{ km s}^{-1}$ . The average solar wind speed across the ICME1 leading edge is about  $504 \text{ km s}^{-1}$ . Comparison between the near-Earth speed ( $\sim 750 \text{ km s}^{-1}$ ), the transit speed ( $\sim 708 \text{ km s}^{-1}$ ), and the speed at *Ulysses* ( $\sim 504 \text{ km s}^{-1}$ ) indicates that ICME1 underwent a gradual deceleration when it propagated from the Earth to *Ulysses*. The major deceleration occurred from the Sun to 1 au when we

compare these speeds with the LASCO speed near the Sun ( $\sim 1300 \text{ km s}^{-1}$ ).

We identify the second ICME (ICME2) by combining the increased alpha-to-proton density ratio, depressed proton temperature, and smooth magnetic field. ICME2 is likely the in situ counterpart of the 2005 May 13 CME (CME2). The CME2-driven shock disappeared at *Ulysses*. The average speed across the ICME2 leading edge is about  $552 \text{ km s}^{-1}$ . Again, the major deceleration of the CME occurred during transit from the Sun to 1 au by comparing the LASCO speed near the Sun ( $\sim 2485 \text{ km s}^{-1}$ ), the shock speed near the Earth ( $\sim 950 \text{ km s}^{-1}$ ), and the speed at *Ulysses* ( $\sim 552 \text{ km s}^{-1}$ ), and thereafter ICME2 experienced a gradual deceleration. There is likely an interaction between the two ICMEs at *Ulysses* as the density and temperature are enhanced in the region between the two ICMEs and the speed of the ICME2 leading edge is larger than that of ICME1. The second ICME may thus have had an extra deceleration by interacting with the first one. However, it is difficult to know whether the two ICMEs have merged or not at *Ulysses* given the one-dimensional nature of the in situ measurements.

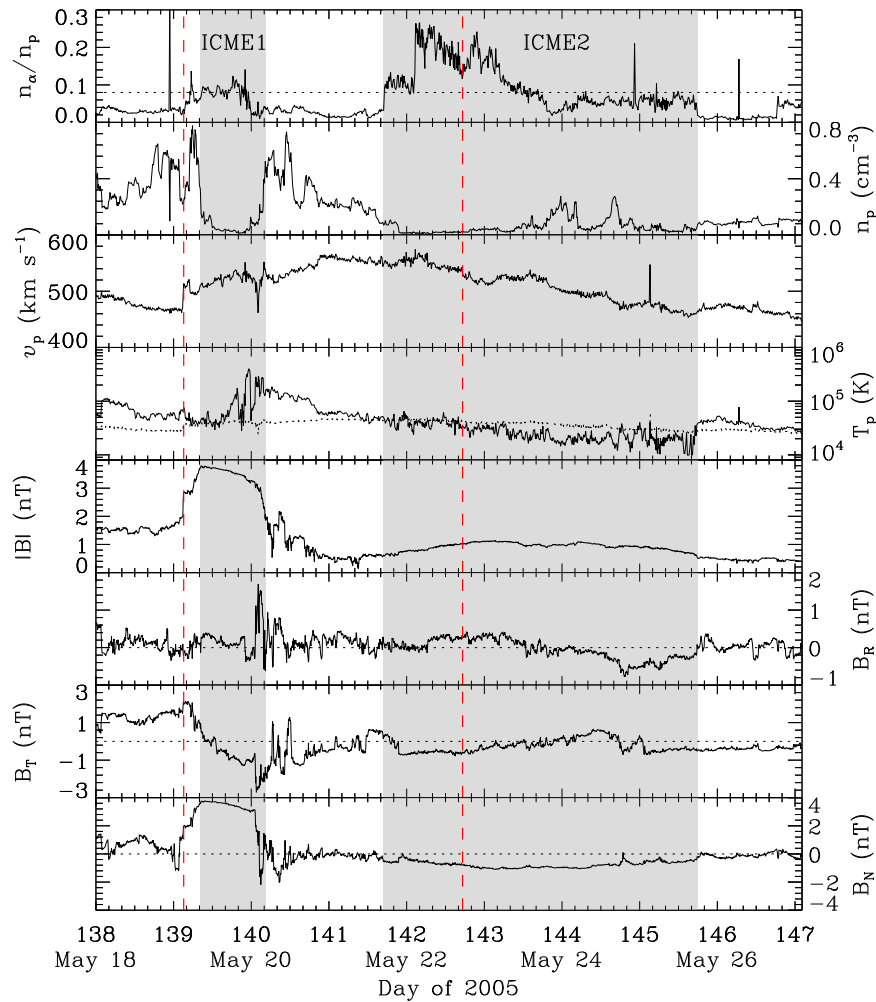


**Figure 6.** Solar wind measurements at *Ulysses*, similar to Figure 4. The dotted curve in the fourth panel is the expected proton temperature from the observed speed by taking into account the temperature–distance gradient ( $R^{-0.7}$ ; Liu et al. 2005). The first red vertical dashed line marks the arrival time of a shock-like structure, and the second one marks the arrival time of the MHD model-predicted shock for CME2.

### 3.3. CME/Shock Interplanetary Propagation

We use a 1D MHD model (Wang et al. 2000) with the solar wind disturbances observed at *Wind* as input, in order to show whether the observations at the Earth and *Ulysses* are consistent with the propagation of the ICMEs. This MHD model assumes spherical symmetry since the in situ solar wind measurements are one-dimensional (e.g., Wang et al. 2001; Richardson et al. 2002, 2005, 2006; Liu et al. 2006a, 2008, 2011; Du et al. 2007). Figure 7 shows the solar wind speed output from the MHD model at certain distances, and the observed ones at *Wind* and *Ulysses*, respectively. The streams associated with ICMEs are still persistent during transit from 1 au to *Ulysses*. A shock forms from the stream associated with ICME1 and is coincident with the shock-like structure observed at *Ulysses*. The predicted arrival time at *Ulysses* is only about 0.7 hr earlier than observed. The time difference ( $\sim 0.7$  hr) is much smaller than the propagation time from *Wind* to *Ulysses* ( $\sim 240$  hr), so the shock-like structure is well tracked by the MHD model. The predicted arrival time of the ICME2 shock at *Ulysses* is about 19:12 UT on May 22, which is about 26 hr later than that of the ICME2 leading edge. Note that the ICME2 shock is missing from the *Ulysses* measurements. The model stream shows an enhanced speed compared with the observed speed within ICME2 at *Ulysses*, but is generally consistent with the ICME2

interval at *Ulysses*. In summary, the model gives a better agreement for ICME1 than for ICME2, which is probably due to the smaller longitudinal separation between the Earth and *Ulysses* during the time of CME1 (Figure 1).

Type II radio bursts can be used to track a shock from the Sun out to 1 au and fill the vacancy of direct solar wind plasma observations (e.g., Reiner et al. 2007; Liu et al. 2008). Figure 8 provides an overview of the radio dynamic spectrum associated with the 2005 May 13 CME (CME2). No clear type II burst associated with the 2005 May 6 CME (CME1) was observed. An intense complex type III radio burst started at about 16:45 UT on May 13, which was almost coincident with the peak of the soft X-ray flux. Lin et al. (1973) suggest that a type III radio burst is caused by electron beams escaping from the flaring region. Such an intense type III burst is a sign of a major CME on the Sun (Reiner et al. 2001). Type II radio bands at the fundamental plasma frequency were observed from about 17:00 UT to 18:50 UT on May 13. After about 19:00 UT on May 13, diffuse type II radio bursts were mainly observed at the harmonic plasma frequency until the arrival of the shock at 1 au on May 15. The type II burst supports our association between the May 13 CME and the ICME at 1 au.

The plasma frequency,  $f_p$  (kHz) =  $8.97\sqrt{n(\text{cm}^{-3})}$ , can be converted to heliocentric distance  $r$  (in units of au) through the



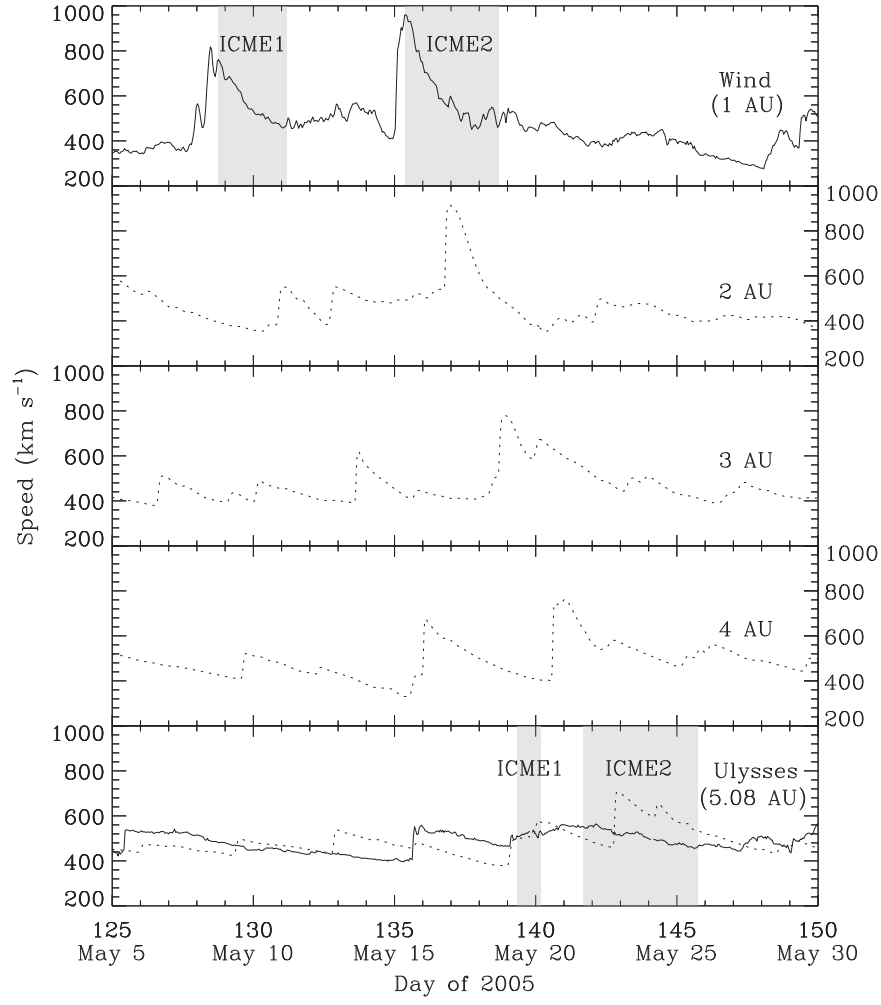


**Figure 7.** Evolution of solar wind speeds from *Wind* to *Ulysses* via the 1D MHD model. All of the panels have the same scales. The solid curves show the solar wind speeds at *Wind* and *Ulysses*, and the dotted curves denote the predicted speeds at 2, 3, 4, and 5.08 au. The shaded regions represent the observed ICME intervals at *Wind* and *Ulysses*.

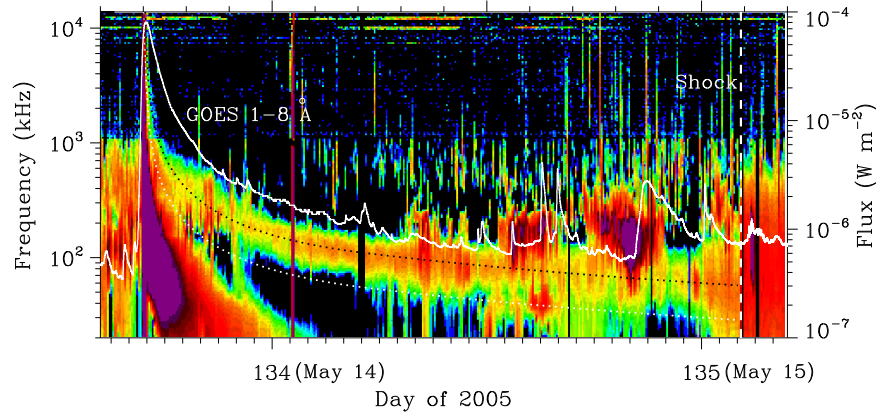


**Figure 8.** Dynamic spectrum (colors) associated with the 2005 May 13 CME from *Wind* WAVES and flare X-ray flux (white curve) from *GOES 12*. The vertical dashed line indicates the arrival time of the shock at the Earth. The black dotted curve represents the best fit of the type II band at the second harmonic plasma frequency, and the white dotted curve is obtained by dividing the best fit by a factor of 2.

Leblanc density model (Leblanc et al. 1998):

$$n = \frac{n_0}{7.2} (ar^{-2} + br^{-4} + cr^{-6}) \text{ cm}^{-3}, \quad (2)$$

where  $a = 7.2$ ,  $b = 1.95 \times 10^{-3}$ ,  $c = 8.1 \times 10^{-7}$ , and  $n_0$  is the electron density near the Earth in units of  $\text{cm}^{-3}$ . Combining

the frequency drift of the type II radio burst and the shock parameters at the Earth, we can obtain a height–time profile of the shock within 1 au. We adopt a kinematic model similar to the approach of Liu et al. (2008), Gopalswamy et al. (2001a), and Reiner et al. (2007). The model assumes that the shock has an initial speed  $v_0$  near the Sun, a constant deceleration  $a$  with a



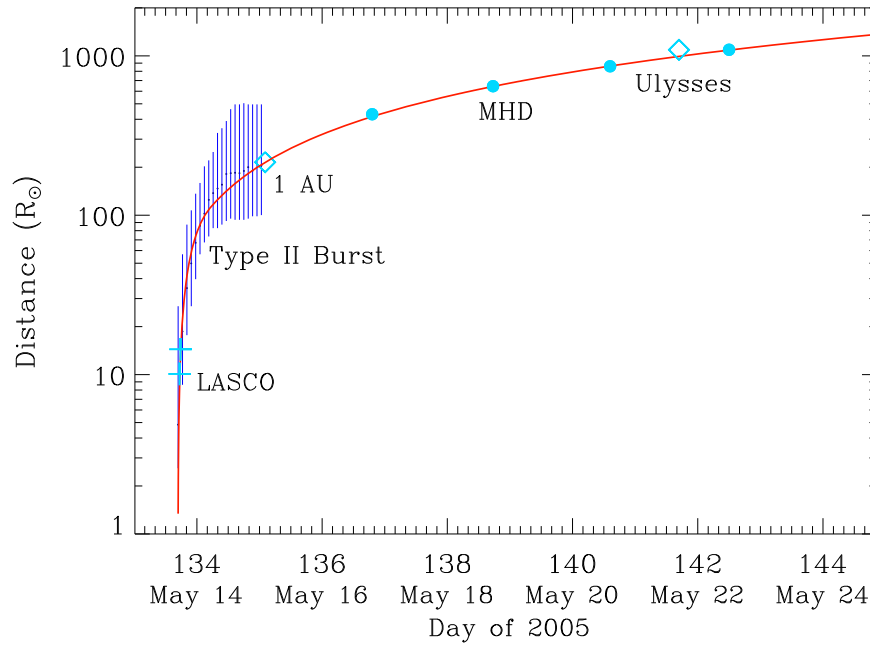


**Figure 9.** Height–time profile (red solid curve) of the CME2-driven shock determined from the frequency drift of the type II radio burst and 1 au shock parameters (where  $R_{\odot}$  is the solar radius). The two crosses are the distances obtained from the GCS model based on the LASCO coronagraph observations. The small black dots with blue error bars indicate the distances obtained from the type II radio burst based on the Leblanc density model. The error bars are acquired according to the bandwidth of the type II radio burst. The two diamonds show the distances of *Wind* and *Ulysses* when the shock and the ICME2 leading edge arrived there, respectively. The large blue dots denote the shock arrival times at 2, 3, 4, and 5.08 au (*Ulysses*) predicted by the MHD model.

deceleration time period  $t_1$ , and a subsequent constant speed  $v_s$ . It does not include an acceleration phase, so its deceleration profile can be considered as an average over the acceleration and rapid deceleration stages in Liu et al. (2013). The kinematic model of the shock can be expressed as

$$r = \begin{cases} d + v_s(t - t_T) + a\left(\frac{1}{2}t^2 + \frac{1}{2}t_1^2 - t_1t\right), & t < t_1, \\ d + v_s(t - t_T), & t \geq t_1, \end{cases} \quad (3)$$

where  $d = 1$  au and  $v_0 = v_s - at_1$ . The initial speed  $v_0$  is determined from LASCO observations ( $\sim 2485$  km s $^{-1}$ ). The shock speed  $v_s$  and the transit time  $t_T$  can be calculated from the in situ measurements at *Wind*. The model has two free parameters ( $n_0$  and  $a$ ). We select the harmonic plasma frequencies of the type II radio burst and then fit the frequencies using the kinematic model. We adjust  $n_0$  for the fit and find that a value of  $n_0 = 10$  cm $^{-3}$  can yield a best fit that simultaneously matches the type II band and the shock parameters at 1 au. Two curves at the fundamental and harmonic plasma frequencies are obtained from the best fit, as shown in Figure 8. The fit is consistent with the type II radio band at the harmonic frequency very well. The fit gives a constant deceleration  $a \approx -35.7$  m s $^{-2}$  and a deceleration time period of about 12.23 hr with a deceleration cessation distance of about 0.52 au ( $\sim 112 R_{\odot}$ ) from the Sun.

Figure 9 shows the distances obtained from the GCS modeling of the LASCO images, the frequency drift of type II radio burst, in situ measurements at *Wind* and *Ulysses*, and MHD model output. We extend the fit in order to show whether it matches the distances beyond 1 au. The fit is consistent with the GCS distances near the Sun and MHD model output outside 1 au, although it is obtained from only the type II burst and 1 au shock parameters. The curve is a little lower than the

*Ulysses* location but not significantly. Again, this is likely due to the longitudinal and latitudinal separations between the Earth and *Ulysses*, possible different solar wind backgrounds, and changes in the CME/shock structure. This height–time curve is generally consistent with the rapid deceleration and then gradual deceleration phases found by Liu et al. (2013) for fast CMEs ( $>1000$  km s $^{-1}$ ). The deceleration cessation distance ( $\sim 112 R_{\odot}$ ) is larger than that of Liu et al. (2013,  $\leq 80 R_{\odot}$ ), but this depends on the coronal and solar wind background and may thus vary.

#### 4. Summary and Discussion

We have analyzed the evolution of two geo-effective CMEs in the heliosphere, which occurred on 2005 May 6 and 13, combining *SOHO*/LASCO coronagraph observations, frequency drift of the type II radio burst measured by *Wind* WAVES (only for the second CME), and in situ measurements at *Wind*, *ACE*, and *Ulysses* with modeling techniques. This work provides insights into the propagation characteristics of CMEs from the Sun far into interplanetary space, as well as space weather forecasting. The results are summarized and discussed as follows.

Comparison between the CME speed near the Sun, the speed at the Earth, and finally the speed at *Ulysses* ( $\sim 5.08$  au) indicates that both of the CMEs had their major deceleration take place inside 1 au and thereafter underwent a gradual deceleration. This is consistent with the general picture of the Sun-to-Earth propagation profile of fast CMEs discovered by Liu et al. (2013) using *STEREO* wide-angle imaging observations, i.e., a rapid deceleration before reaching 1 au followed by a gradual deceleration or a roughly constant speed (note that we did not include the acceleration phase here due to the limitation of the present observations). Based on the type II radio burst and the 1 au shock parameters, we obtain a best fit of the

height–time curve for the 2005 May 13 CME (CME2) and find that the rapid deceleration of CME2 ceased at about  $112 R_{\odot}$ . This gives further evidence for the rapid deceleration of fast CMEs before reaching 1 au, although the cessation distance of the rapid deceleration is somewhat larger than those in Liu et al. (2013). The best fit also matches CME distances near the Sun and MHD model output at different distances, and is roughly consistent with the arrival of the ICME2 leading edge at *Ulysses*. This indicates the application of a simple kinematic model to a large range of distances (from the Sun to about 5 au), which is important for space weather forecasting. Comparison of the kinematics between the two CMEs suggests that the faster the CME, the larger the deceleration within 1 au. As the deceleration is due to interactions with the ambient solar wind, this result confirms that CMEs tend to comove with the ambient solar wind before reaching 1 au (Lindsay et al. 1999; Gopalswamy et al. 2001a; Liu et al. 2016).

The results also suggest that the two CMEs may start to interact around 5 au at *Ulysses*, although their eruption times on the Sun were well separated (by about a week). There is no evidence that the two CMEs interacted with each other near the Earth, as can be seen from the in situ measurements at *Wind* and *ACE*. When the second CME occurred, the first CME had already passed beyond 1 au. They may interact with each other far into interplanetary space, due to the fact that the ARs were at similar longitudes with respect to the Earth/*Ulysses* and CME2 is faster than CME1. The result that the two CMEs interacted in deep interplanetary space indicates the “fate” of CMEs in the heliosphere, i.e., different CMEs may eventually merge and form merged interaction regions in the outer heliosphere with their identities lost (e.g., Burlaga 1984; Richardson et al. 2002; Liu et al. 2014b).

Two intense geomagnetic storms occurred with minimum  $D_{st}$  values of  $-110$  nT and  $-247$  nT, respectively. For the first case without a shock, the geomagnetic storm was induced by the southward field components in the CIR ahead of the ICME (Zhang et al. 2007). The ICME may have contributed to the geomagnetic storm by compressing the CIR from behind. For the second case with a preceding shock, the geomagnetic storm was primarily caused by the southward field components between the shock and ejecta. Both cases stress the critical role of the sheath region in geomagnetic storm generation.

The research was supported by the Recruitment Program of Global Experts of China, the NSFC under grant 41374173, and the Specialized Research Fund for State Key Laboratories of China. We acknowledge the use of data from *SOHO*, *GOES*, *Wind*, *ACE*, *Ulysses*, and the  $D_{st}$  index from WDC in Kyoto.

## References

- Bisi, M. M., Breen, A. R., Jackson, B. V., et al. 2010, *SoPh*, **265**, 49
- Burlaga, L. F. 1984, *SSRv*, **39**, 255
- Cane, H. V., Kahler, S. W., & Sheeley, N. R., Jr. 1986, *JGR*, **91**, 13321
- Cash, M. D., Biesecker, D. A., Pizzo, V., et al. 2015, *SpWea*, **13**, 611
- Cheng, X., Zhang, J., Ding, M. D., Liu, Y., & Poomvises, W. 2013, *ApJ*, **763**, 43
- Cremades, H., Iglesias, F. A., St., Cyr, O. C., et al. 2015, *SoPh*, **290**, 2455
- Du, D., Wang, C., & Hu, Q. 2007, *JGRA*, **112**, A09101
- Du, D., Zuo, P. B., & Zhang, X. X. 2010, *SoPh*, **262**, 171
- Dungey, J. W. 1961, *PhRvL*, **6**, 47
- Gonzalez, W. D., Joselyn, J. A., Kamide, Y., et al. 1994, *JGR*, **99**, 5771
- Gonzalez-Esparza, A., & Aguilar-Rodriguez, E. 2009, *AnGeo*, **27**, 3957
- Gopalswamy, N. 2010, *ApSSP*, **18**, 53
- Gopalswamy, N., Lara, A., Lepping, R. P., et al. 2000, *GeoRL*, **27**, 145
- Gopalswamy, N., Lara, A., Yashiro, S., Kaiser, M. L., & Howard, R. A. 2001a, *JGR*, **106**, 29207
- Gopalswamy, N., Yashiro, S., Kaiser, M. L., Howard, R. A., & Bougeret, J.-L. 2001b, *ApJL*, **548**, L91
- Hu, H., Liu, Y. D., Wang, R., Möstl, C., & Yang, Z. 2016, *ApJ*, **829**, 97
- Kataoka, R., Shiota, D., Kilpua, E., & Keika, K. 2015, *GeoRL*, **42**, 5155
- Leblanc, Y., Dulk, G. A., & Bougeret, J.-L. 1998, *SoPh*, **183**, 165
- Lin, R. P., Evans, L. G., & Fainberg, J. 1973, *ApL*, **14**, 191
- Lindsay, G. M., Luhmann, J. G., Russell, C. T., & Gosling, J. T. 1999, *JGR*, **104**, 12515
- Liu, Y., Luhmann, J. G., Bale, S. D., & Lin, R. P. 2011, *ApJ*, **734**, 84
- Liu, Y., Luhmann, J. G., Müller-Mellin, R., et al. 2008, *ApJ*, **689**, 563
- Liu, Y., Richardson, J. D., & Belcher, J. W. 2005, *P&SS*, **53**, 3
- Liu, Y., Richardson, J. D., Belcher, J. W., et al. 2006a, *JGRA*, **111**, A12S03
- Liu, Y., Richardson, J. D., Belcher, J. W., Kasper, J. C., & Skoug, R. M. 2006b, *JGRA*, **111**, A09108
- Liu, Y., Thernisien, A., Luhmann, J. G., et al. 2010, *ApJ*, **722**, 1762
- Liu, Y. D., Hu, H., Wang, C., et al. 2016, *ApJS*, **222**, 23
- Liu, Y. D., Hu, H., Wang, R., et al. 2015, *ApJL*, **809**, L34
- Liu, Y. D., Luhmann, J. G., Kajdič, P., et al. 2014a, *NatCo*, **5**, 3481
- Liu, Y. D., Luhmann, J. G., Lugaz, N., et al. 2013, *ApJ*, **769**, 45
- Liu, Y. D., Luhmann, J. G., Möstl, C., et al. 2012, *ApJL*, **746**, L15
- Liu, Y. D., Richardson, J. D., Wang, C., & Luhmann, J. G. 2014b, *ApJL*, **788**, L28
- Lopez, R. E., & Freeman, J. W. 1986, *JGR*, **91**, 1701
- Lugaz, N., Farrugia, C. J., Davies, J. A., et al. 2012, *ApJ*, **759**, 68
- Manchester, W. B., IV, van der Holst, B., & Lavraud, B. 2014, *PPCF*, **56**, 064006
- Mishra, W., Srivastava, N., & Chakrabarty, D. 2015, *SoPh*, **290**, 527
- Reiner, M. J., Kaiser, M. L., & Bougeret, J.-L. 2001, *JGR*, **106**, 29989
- Reiner, M. J., Kaiser, M. L., & Bougeret, J.-L. 2007, *ApJ*, **663**, 1369
- Richardson, I. G. 2014, *SoPh*, **289**, 3843
- Richardson, I. G., & Cane, H. V. 1993, *JGR*, **98**, 15
- Richardson, I. G., & Cane, H. V. 1995, *JGR*, **100**, 23397
- Richardson, I. G., & Cane, H. V. 2004, *JGRA*, **109**, A09104
- Richardson, J. D., Liu, Y., Wang, C., et al. 2006, *GeoRL*, **33**, L23107
- Richardson, J. D., Paularena, K. I., Wang, C., & Burlaga, L. F. 2002, *JGRA*, **107**, 1041
- Richardson, J. D., Wang, C., Kasper, J. C., & Liu, Y. 2005, *GeoRL*, **32**, L03S03
- Sheeley, N. R., Walters, J. H., Wang, Y.-M., & Howard, R. A. 1999, *JGR*, **104**, 24739
- Temmer, M., & Nitta, N. V. 2015, *SoPh*, **290**, 919
- Temmer, M., Vršnak, B., Rollett, T., et al. 2012, *ApJ*, **749**, 57
- Thernisien, A., Vourlidas, A., & Howard, R. A. 2009, *SoPh*, **256**, 111
- Thernisien, A. F. R., Howard, R. A., & Vourlidas, A. 2006, *ApJ*, **652**, 763
- Tsurutani, B. T., & Gonzalez, W. D. 1997, *GMS*, **98**, 77
- Wang, C., Richardson, J. D., & Gosling, J. T. 2000, *JGR*, **105**, 2337
- Wang, C., Richardson, J. D., & Paularena, K. I. 2001, *JGR*, **106**, 13007
- Woo, R. 1988, *JGR*, **93**, 3919
- Woo, R., Armstrong, J. W., Sheeley, N. R., Jr., et al. 1985, *JGR*, **90**, 154
- Yurchyshyn, V., Liu, C., Abramenko, V., & Krall, J. 2006, *SoPh*, **239**, 317
- Zhang, J., Richardson, I. G., Webb, D. F., et al. 2007, *JGRA*, **112**, A10102